

RESEARCH ARTICLE | AUGUST 29 2023

Thermionic emission of a tungsten surface in high heat flux plasma: PIC simulations **FREE**

J. Moritz ; S. Heuraux ; N. Lemoine ; M. Lesur ; E. Gravier ; F. Brochard ; L. Marot ; P. Hiret 



Physics of Plasmas 30, 083514 (2023)

<https://doi.org/10.1063/5.0160767>



View
Online



Export
Citation

CrossMark

Articles You May Be Interested In

A consistent interface between PIC-simulations

AIP Conference Proceedings (February 1997)

PIC/MCC analysis of a photoresonance plasma sustained in a sodium vapor

Physics of Plasmas (July 2017)

The role of noise in PIC and Vlasov simulations of the Buneman instability

Physics of Plasmas (December 2021)

Thermionic emission of a tungsten surface in high heat flux plasma: PIC simulations

Cite as: Phys. Plasmas **30**, 083514 (2023); doi: 10.1063/5.0160767

Submitted: 5 June 2023 · Accepted: 6 August 2023 ·

Published Online: 29 August 2023



View Online



Export Citation



CrossMark

J. Moritz,^{1,a)} S. Heurax,¹ N. Lemoine,¹ M. Lesur,¹ E. Gravier,¹ F. Brochard,¹ L. Marot,² and P. Hirt²

AFFILIATIONS

¹Institut Jean Lamour, UMR 7198 CNRS, Université de Lorraine, Campus Artem, 2 allée André Guinier, 54011 Nancy, France

²Department of Physics, University of Basel, Klingelbergstrasse 82, CH-4056 Basel, Switzerland

^{a)} Author to whom correspondence should be addressed: jerome.moritz@univ-lorraine.fr

ABSTRACT

The surface temperature of a tungsten surface facing hot hydrogen plasma is evaluated, thanks to 1d/3v particle-in-cell simulations in floating wall conditions. At each iteration, the plasma heat flux to the cathode is equalized with the outgoing one, which is due to thermionic emission, surface radiation, and heat conduction through the wall. The thermal conductivity is chosen within the range 35–160 W m⁻¹ K⁻¹ in the different simulations in order to take into account the surface condition. A transition from a cold temperature surface to a hot one arises for a critical thermal conductivity, whose value depends on the plasma parameters. This transition is very abrupt and leads to a space charge limited regime where the thermionic current penetrating the plasma has reached its maximal value and is about three times the Bohm current. Changing the initial conditions in the code, more particularly, the timing of electron emission, can lead to a very different final surface temperature. This history effect and the associated hysteresis are evidenced by means of fluid calculations, which are in a good agreement with the simulation results as well as with previous experimental measurements.

Published under an exclusive license by AIP Publishing. <https://doi.org/10.1063/5.0160767>

I. INTRODUCTION

The plasma–wall interaction is a fundamental issue in fusion devices, and, in particular, for ITER, because high heat fluxes in the tens of MWm⁻² range are expected to hit on parts of the first wall of this large size tokamak. High heat fluxes can lead to the formation of hot spots¹ on plasma-facing components, resulting, for instance, in erosion on the divertor plate material or antenna structures and in the subsequent pollution of the plasma core.

In the ITER scenario, the tungsten (W) mono-blocs are designed at the divertor to withstand a steady state 10 MW/m² heat flux. In a numerical study, Gunn *et al.*² have shown that during this steady state phase, the W surface temperature T_s at the trailing edge of the mono-blocs can reach 1300–1600 K and even above the melting temperature during slow transient reattachment events with a heat flux of the order of 20 MW/m². In misaligned W mono-blocs with different shaping,³ a temperature of the order of 3400 K is expected for a steady state perpendicular heat flux of 31 MW/m². An exposed leading edge receives actually 15 to 60 times more heat loads than a perfectly aligned surface.⁴ Such misalignment of the W mono-blocs has been extensively studied in tokamak facilities under plasma conditions with parallel heat flux of the order of 100 MW/m². Melting of the mono-blocs edges and thermionic

emission was evidenced in several reports.^{5,6} These experimental observations have led to further numerical works emphasizing the importance of sheaths at the vicinity of hot tungsten surfaces in Edge Localized Mode (ELM) phases for modeling the melt motion induced by fast transients.⁷

In this context, thermionic emission of electrons from hot material surfaces is of particular interest, because it deeply changes the energy transmission coefficient through the sheath.^{8,9} On the one hand, thermionic emission can induce a reduction of the sheath voltage, which can prevent plasma species to overcome the sputtering threshold of the surface and suppress the impurity generation by physical sputtering.¹⁰ On the other hand, the expected decrease in the potential drop in the sheath can lead to the enhancement of the heat flux to the wall because a larger amount of hot plasma electrons are allowed to reach the surface. The increased heat flux increases the surface temperature T_s as well as the thermionic current J_s according to the Richardson–Dushman's formula,

$$J_s = AT_s^2 \exp\left(-\frac{B_w}{k_b T_s}\right), \quad (1)$$

with A being the Dushman's constant, and B_w being the electron work function, which both depend on the surface material. For tungsten,¹¹

$A = 60 \times 10^4 \text{ Am}^{-2}\text{K}^{-2}$ and $B_w = 4.55 \text{ eV}$. This enhancement of J_s in turn increases the plasma heat flux again; the instability finally ends up when an equilibrium surface temperature is reached.¹²

Surface heating induces at the same time not only the desorption of hydrogen atoms trapped at the material vacancies¹³ but also the sublimation of the material itself.¹⁴ The hydrogen atoms, if ionized near the surface, increase locally the density of the main plasma, and the ionized metallic vapor creates a secondary plasma in front of the spot. While the return of part of the material vapor to the surface contributes to its over-heating,¹⁵ the presence of a denser secondary plasma allows for an enhancement of the thermionic current. Both phenomena are envisaged as the origin of unipolar arcs, which drain a very large amount of current circulating from the wall to the plasma.^{16,17}

The emitted current is indeed strongly limited by space charge effects. The first model explaining this electrostatic phenomenon was by Child¹⁸ in 1911, which has been extended by Langmuir¹⁹ two years later in order to explain the saturation of the thermionic current with the temperature of an emitting filament. Actually, when electrons are emitted without initial velocity from a cathode in vacuum, as soon as the electric field vanishes at the surface due to the accumulation of negative charges, the current is limited. This basic assumption allows the derivation of the well-known Child–Langmuir expression of the limited current,

$$J_s^* = \frac{4\epsilon_0}{9} \sqrt{\frac{2e}{m}} \frac{V^{3/2}}{L^2}, \quad (2)$$

where J_s^* is the maximum charge current, V is the applied voltage, e and m are the electron charge and mass, respectively, and L is the distance between electrodes.

Although Eq. (2) is theoretically only applicable to vacuum, it is used in plasma physics in order to derive the variation of the sheath size with respect to a wall potential,^{20,21} which is important for instance in Langmuir probe measurements and their interpretation. However, as sheaths are positive-space-charged regions built up in surface vicinity in order to balance the flow of particles, they modify substantially the assumptions used to derive Eq. (2). That is why several authors have extended the Child–Langmuir model by taking into account the presence of this thin positive charged layer extending over a few Debye lengths (λ_d) and evaluated the effect of an emitted electron current J_s , which would tend to neutralize it. Models have been derived in floating^{8,22,23} as well as under biased wall conditions.^{24–26} Both theoretical approaches lead to the same conclusion: above a maximum thermionic current J_s^* , the accumulation of negative charges at the wall vicinity induces a non-monotonic variation of the plasma potential; the electric field cancels close to the surface. In this situation, the wall is covered up by a double layer, with a potential well (a virtual cathode), which regulates the electron current. In other words, if the space charge limited regime is not yet reached, J_s is given by the Richardson–Dushman formula [Eq. (1)], otherwise the current is limited and the current penetrating the plasma is J_s^* even if T_s is still increased. Then, the virtual cathode reflects the current $J_s - J_s^*$.

The effect of the thermionic emission onto the sheath structure has been also studied thanks to particle-in-cell (PIC) simulations, where J_s was varied by setting the surface temperature T_s according to the Richardson–Dushman’s equation. The authors studied the variation of the sheath size,²⁷ the potential drop in the sheath and the

saturation of the thermionic current penetrating the plasma with respect to T_s , the formation of the virtual cathode,²⁸ as well as the effect of electron redeposition in the presence of a tilted magnetic field.²⁹

In this study, we propose to extend these previous numerical works by determining self-consistently the surface temperature of a cathode facing a hot hydrogen plasma by using PIC simulations corresponding to unmagnetized plasma cases. This can be achieved by balancing the heat fluxes at the wall coming from the plasma, i.e., the heat flux deposited by ions and electrons (kinetic and potential recombination or adsorption energy) and conducted away from the surface, i.e., the heat flux carried out by conduction, radiation, and thermionic emission. Our goal is to be able to estimate the surface temperature of a tungsten wall, because this material is foreseen as a good candidate material for divertor target plates in future fusion reactors, thanks to its low tritium retention and low sputtering yield,³⁰ with respect to different plasma conditions and surface properties. We focus in this study on thermionic emission only, where the amplitude of the emitted current relies on the surface temperature. Other effects can strengthen J_s though, such as the Schottky correction to the material work function³¹ or secondary electron emission (see, e.g., Ref. 7 and references therein). If included in our numerical model, these effects would lead to an increase in the emitted current with respect to the one calculated with the Richardson formula and have an impact on the temperature at which the sheath limited regime appears. We also exclude the detached divertor regime from this study since it requires introducing a large set of additional mechanisms, such as ionization processes, charge-exchange collisions, and neutral particle recycling as mentioned in Refs. 32 and 33, which is out of the scope of this paper.

In the first part of the paper, we present the simulated system, and we detail the way the calculations are performed, especially how the surface temperature can be determined in the steady state. Then we focus on the numerical results, discussing the sheath formation during the first time iterations as well as the density and potential spatial variations in the presence of thermionic emission. We also analyze the variation of the surface temperature, the sheath potential, and the emitted current with respect to an increasing surface thermal conductivity in two plasma conditions. We finally present a simple fluid model in order to explain qualitatively and quantitatively the numerical results and relate them to the bifurcation S curves obtained and already evidenced by other authors in fluid calculations.

II. PIC SIMULATIONS

A. Simulated system

In our 1d/3v PIC simulations, a semi-infinite plasma is bounded by a grounded conductive wall at $x = 0$, i.e., with a surface potential $\phi(0) = 0$. The right boundary condition at $x = L = 100\lambda_d$ is such that the electric field cancels, $\phi'(L) = 0$. Particles move along the x axis until they reach one of the simulated system boundaries. At $x = L$, they are simply reflected and return back into the plasma with a velocity that is reset in the initial Maxwellian velocity distribution. As there is not net current at $x = L$, there should be a balance of the charges at the surface in order to preserve the plasma quasi-neutrality (floating wall conditions).

At $x = 0$, hydrogen ions recombine with electrons extracted from the wall material and are recycled as neutrals in the plasma. Though the wall material is at a lower potential than the plasma, an important electron flux can reach the wall, so that electrons arriving at $x = 0$ are

absorbed by the surface. There is no reflection of the plasma particles or energy at the wall in our simulations. The ion neutralization at $x=0$ or the electron absorption are sources of the cathode spot heating, which will be detailed in Subsection II B. At each iteration, a number of thermo-emitted electrons is calculated, thanks to the Richardson–Dushman formula [Eq. (1)].

Electrons are deposited at the surface at $x=0$ and are eventually accelerated toward the plasma due to a strong negative electric field in the sheath region. Their initial kinetic energy is set to be $k_b T_s$, and their initial velocity vector is distributed over one hemisphere in order to provide an isotropic angular distribution as proposed in Ref. 34 for secondary electron injection. The grid size is chosen as small as $dX = 0.0125 \lambda_d$ in order to describe accurately the wall vicinity and to track the motion of the emitted electrons with great precision. The time step is then picked up according to the grid size, due to the Courant condition, i.e., $v_{te} \times dt = 0.25 \times dX$, where v_{te} is the electron thermal velocity. This procedure ensures that most electrons cannot travel across an entire cell dX during a single dt .

We tagged during the simulations the emitted electrons vs the plasma ones in order to sort them. When a thermionic electron has traveled throughout the plasma and reached the right boundary, it is reflected back into the plasma (as the other particles) and its velocity reset in the initial Maxwell's distribution: then the electron is categorized as a plasma one. Tagging the emitted electrons is also very helpful for determining precisely the maximum emitted current J_s^* at the surface. For that purpose, it is indeed necessary to ascribe if one electron hitting the wall is from the plasma or a previous emitted one reflected by the virtual cathode.

Collisions between charged particles or with neutrals are not taken into account, nor ionization or recombination within the plasma. As in our previous studies based on PIC simulations,³⁵ the number of ions was kept constant during the calculations: once a single ion reaches the left boundary (the wall material), a couple ion + electron is injected randomly within the simulated plasma according to a uniform law in order to preserve quasi-neutrality. This injection method is known to distort the velocity distribution functions^{36–38} and to induce a cooling of the plasma with respect to the nominal loaded one. As the different potential drops in the plasma, i.e., in the sheath or the pre-sheath, depend on the electron temperature, as well as the amplitude of the ion acoustic velocity c_s , we determined the final temperatures of the plasma when the simulations are completed. For that purpose, the (x, v_x) phase space of the plasma species was saved at the end of the simulations. Then the plasma was arbitrarily divided in ten slabs, whose length was $10 \lambda_{db}$ and the temperature calculated on the first one, in a region encompassing the sheath by determining the average kinetic energy of the plasma slab.

The simulations are run for $300 \times 2\pi/\omega_{pe}$ periods, with ω_{pe} being the electron plasma pulsation, which is long enough for the sheath to be established (ω_{pe}^{-1} is its characteristic time). For such a simulation window, hydrogen ions can travel across half of the plasma size at their thermal velocity, so that all the ion velocity distribution has passed through the sheath extending over a few λ_{db} and contributed to the surface heating, during this time frame. We check at the end of the simulations that the steady state is reached for the heat flux to the surface or the space potential at its vicinity. The different quantities, such as the space potential or the particles' density are averaged over the last $50 \times 2\pi/\omega_{pe}$. The emitted and plasma electrons as well

as ion fluxes at the wall are recorded every hundred iterations and also averaged over the last 50 periods for further use and interpretation. Note that the time step according to our plasma properties and the grid size dX used can be as small as 2.5×10^{-14} s, for a total simulated time of 0.015 μ s.

B. Heat flux balance at the surface

For each time iteration, the heat flux deposited by ions and electrons on the cathode surface is calculated during the PIC simulations; it consists of the kinetic energy of the particles added to the energy terms due to ion neutralization and electron absorption. The heat flux from the plasma to the wall writes

$$Q_p = \Gamma_i(E_i - B_w) + \Gamma_e B_w + Q_i^k + Q_e^k, \quad (3)$$

where Q_i^k and Q_e^k are the ion and electron kinetic energy fluxes, Γ_i and Γ_e are the ion and electron fluxes at the surface, and $E_i = 13.6$ eV is the recombination energy for hydrogen. The hydrogen plasma density being chosen within the range $1 - 10 \times 10^{18} \text{ m}^{-3}$ in the PIC simulations with $k_b T_i = k_b T_e = 10$ eV, conditions met in the divertor plasmas of medium size tokamaks in attached mode such as JET or WEST,^{39,40} and assuming $\Gamma_e = \Gamma_i \simeq n_0 c_s$, one can expect a particle flux of the order of 10^{22} to $10^{23} \text{ s}^{-1} \text{ m}^{-2}$ and a heat flux density that can reach 1 MW m^{-2} for the first two terms of Eq. (3).

The heat conducted away from the cathode surface is due to emission of electrons, surface radiation, and heat conduction; all these terms depend on the surface temperature T_s , which is to be determined. It can be calculated as

$$Q_c = \frac{J_s(T_s)}{e} (B_w + k_b T_s) + \epsilon \sigma T_s^4 + \frac{\kappa}{t} (T_s - T_0), \quad (4)$$

where ϵ is the emissivity of the surface, σ is the Stefan–Boltzmann constant, κ is the thermal conductivity, and t is the wall thickness (1 cm in the present study).

An average $\epsilon = 0.25$ is chosen for all simulation runs,⁴¹ while different values of κ are tested from 0 up to $140 \text{ W m}^{-1} \text{ K}^{-1}$. A typical value for the tungsten thermal conductivity⁴² at room temperature ($T_0 = 300 \text{ K}$) would be $180 \text{ W m}^{-1} \text{ K}^{-1}$ and would decrease down to $90 \text{ W m}^{-2} \text{ K}^{-1}$ within a temperature range of 3000–4000 K. However, a conductivity as low as $10 \text{ W m}^{-1} \text{ K}^{-1}$ is expected for an altered tungsten surface previously submitted to plasma irradiation.⁴³ It is known indeed that the presence of bubbles (empty or filled with He/D) in the tungsten lattice decreases its thermal conductivity.⁴⁴ Finally, micro-crackings in polycrystalline materials can also reduce the thermal conductivity by a factor 3 with respect to the expected value.⁴⁵ It is then worth testing in our plasma simulations a large range of the thermal conductivity to take into account the surface irradiation history corresponding to real divertor W mono-blocs or general targets having different surface conditions.

We neglect in the present study the heat flux due to the material wall evaporation. According to Langmuir,⁴⁶ the rate of evaporation of tungsten at 3500 K is of about $J_{ev} = 2.52 \times 10^{22} \text{ m}^{-2} \text{ s}^{-1}$, which induces a heat flux of the order of $Q_{ev} = J_{ev} \times W_{ev}$, with $W_{ev} = 8 \text{ eV}$ the evaporation energy for W. It leads to $Q_{ev} = 0.032 \text{ MW/m}^{-2}$, which is two orders of magnitude smaller than the surface radiation contribution for the same temperature. Even at 4000 K, assuming the rate of evaporation of Ref. 47, the heat flux due to the wall evaporation is still

quite below the radiation one; Q_{ev} finally reaches the MW/m^{-2} mark for $T_s = 4600 \text{ K}$ and liquid tungsten.

Assuming $Q_p = Q_c$ enables straightforwardly the determination of T_s for the considered time iteration, Q_p being given by the PIC code, and Q_c provided by an analytical expression [Eq. (4)], which only depends on the material properties and on T_s . Then the number of thermionic electrons to be released at the wall can be calculated for the deduced T_s , thanks to Richardson–Dushman formula [Eq. (1)]. Doing so, we suppose that the surface will converge to a final temperature in the steady state, where there is a balance between a stable heat flux coming from the plasma to the surface and conducted away from it, once the sheath and eventually the virtual cathode are established. The determination of the final temperature of the surface with respect to both the cathode and plasma properties is then achieved after the PIC simulations. The average heat flux $\overline{Q_p}$ from the plasma species to the wall has been calculated from the recorded data points on the last $50 \times 2\pi/\omega_{pe}$ periods. Then, Eq. (4) is used with $\overline{Q_p}$ to determine the final T_s . We have implemented this method in order to avoid averaging the temperature deduced at each time iteration.

III. RESULTS

A. Plasma potential, density, and sheath building

The simulated plasma potential profile for seven values of κ in the case of a $5 \times 10^{18} \text{ m}^{-3}$ hydrogen plasma with $k_b T_i = k_b T_e = 35 \text{ eV}$, values close to those found in the scrape-off layer of tokamaks, is shown in Fig. 1(a). When κ decreases, less heat flows through the wall thickness according to Eq. (4), so that the surface temperature is expected to increase, as well as the thermionic current (both properties are presented in Fig. 6). As a result, the electron density in the immediate surface vicinity exhibits a slight augmentation, Fig. 1(d), as compared to the highest thermal conductivity, Fig. 1(c). This phenomenon induces a small decrease in the space charge in the sheath as well as of the potential drop into it until $\kappa = 65 \text{ W m}^{-1} \text{ K}^{-1}$. At this threshold value of heat conductivity, the electron density facing the surface cannot be increased further, and the electric field at the target E_s vanishes for emitted current regulation purpose. It results in a drop of the plasma potential because the system abruptly bifurcates toward another energy minimum. If κ is decreased further, E_s becomes

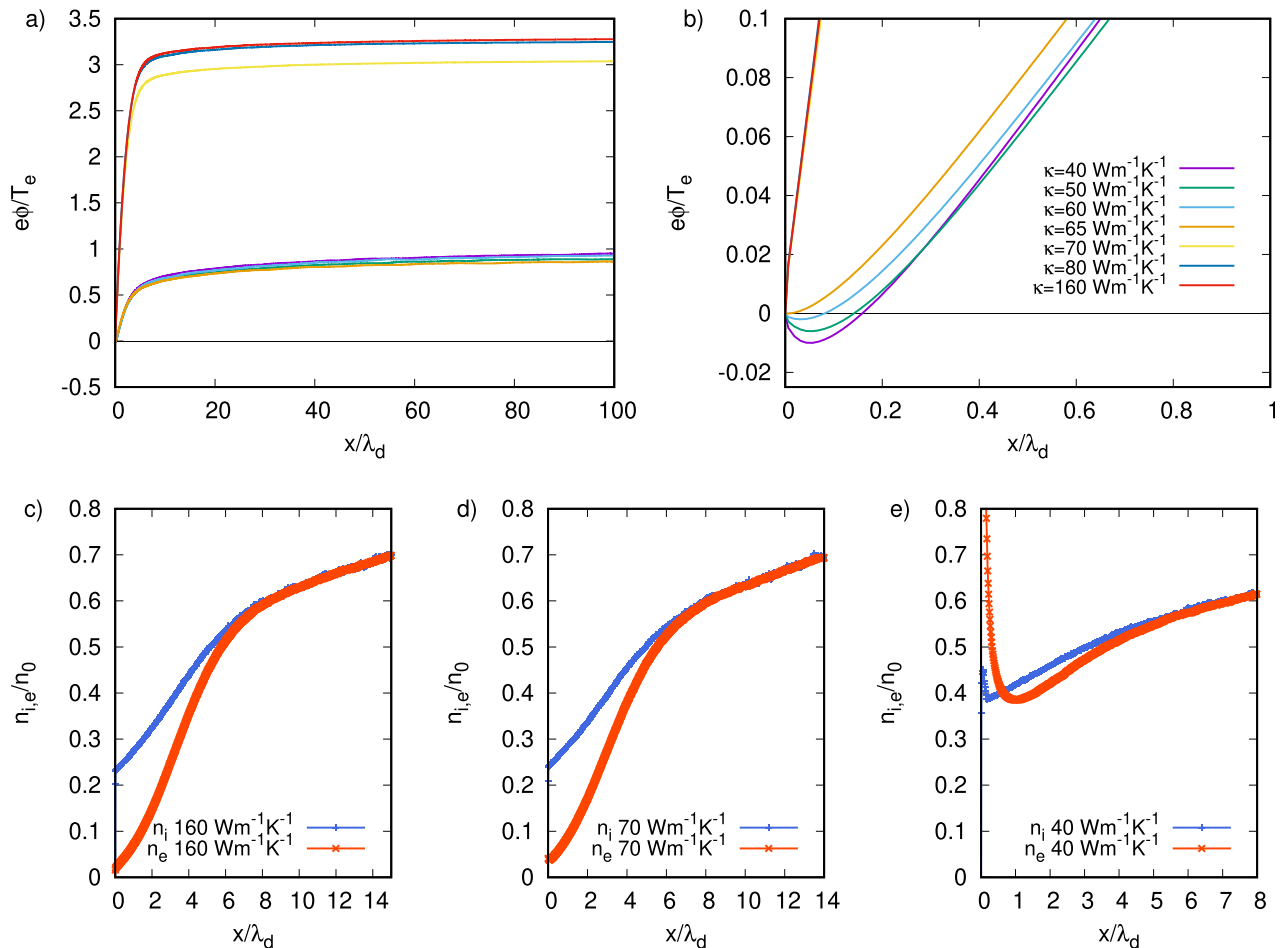


FIG. 1. (a) and (b) Spatial variation of the plasma potential ϕ for seven values of the thermal conductivity κ . The simulation parameters are $n_0 = 5 \times 10^{18} \text{ m}^{-3}$ and $k_b T_i = k_b T_e = 35 \text{ eV}$. The zoom in (b) allows the visualization of the virtual cathode facing the wall for the lowest κ values. (c), (d), and (e) Profiles of the ionic (n_i) and electronic (n_e) density in the surface vicinity for $\kappa = 160, 70,$ and $40 \text{ W m}^{-1} \text{ K}^{-1}$, respectively.

positive, and a virtual cathode builds up close to the wall [Fig. 1(b)]. In this case, the negative charge created by the thermionic emission counterbalances the positive one and a double layer occurs, Fig. 1(e), which characterizes the space charge limited regime.

The building of the sheath and eventually of the double layer arises over the first plasma periods of the simulations. During the first ten or so time iterations, a large flux of electrons reaches the wall because of the absence of a sheath, which leads to a huge heat flux to the cathode, Fig. 2(a). This loss of plasma electrons leads to a positive charge surplus in the near-surface environment. However, because of the heat flux previously received by the wall, its temperature increases [see Fig. 2(c)], resulting in strong thermionic emission: the positive charge surplus is then quickly neutralized by the emitted electrons, destroying the thin sheath. This process of high heat loads followed by strong emission, both large oscillating virtual cathode potential (ϕ_{vc}) and instantaneous surface temperature, is repeated several times until ϕ_{vc} and T_s stabilize and the sheath is completely deployed, Figs. 2(b) and 2(c). As a consequence, the heat flux due to electrons decreases until the steady state is reached, while the ion heat flux increases during the early stages of the simulations because of the building of the sheath potential. Finally, the total heat flux converges to a stable value, which is higher [e.g., for $\kappa = 50 \text{ W m}^{-1} \text{ K}^{-1}$ in Fig. 2(a)] or lower [e.g., for $\kappa = 75 \text{ W m}^{-1} \text{ K}^{-1}$ in Fig. 2(a)] for higher and lower

temperature [respectively, ≈ 3000 and $\approx 1100 \text{ K}$ in Fig. 2(c)]. It is important to notice that even if the surface reaches a relatively cold temperature (without both strong emission and a virtual cathode close to it) in the steady state, during the transient one, it may have experienced high heat loads, as explained above. This history of the surface temperature surface may have a strong impact on the final results of the calculations, as will be emphasized later on in the paper.

In order to determine the sheath entrance location, several approaches are possible. Some authors base this determination on the space-charge amplitude relative to the plasma density at the wall vicinity with a simple criterion such that $n_i(s) - n_e(s) = 0.02 - 0.04 \times n_0$, where s is the sheath size measured from the wall, and n_i and n_e are the ion and electron density.^{48,49} As we have extracted the sheath entrance location when the simulations are completed, we used, as in our previous studies, the Bohm criterion,⁵⁰ i.e., the point where the ion fluid velocity perpendicular to the wall, v_{ix} , reaches the ion acoustic velocity, c_s , where quasi-neutrality breaks down. We also used this sonic point abscissa for estimating the potential drop in the sheath in our simulations.

The spatial variation of v_{ix} (the ion velocity averaged in each cell during the PIC simulations) for five values of the thermal conductivity is depicted in Fig. 3(a). The ions velocity profiles depend on the temperature of the surface, i.e. cold vs hot surface (the corresponding temperatures will be entirely displayed in Fig. 6 and discussed later). Above the thermal conductivity threshold of $65 \text{ W m}^{-1} \text{ K}^{-1}$, ions are accelerated up to c_s , thanks to the pre-sheath potential drop and enter the sheath at $x/\lambda_d = 3.8$, which is the sheath size in this regime. They then experience a large negative electric field in the sheath and reach the wall at a velocity close to $-2 \times c_s$. For smaller values of the thermal conductivity, the thermionic emission induced by the larger surface temperature neutralizes the positive space-charge close to the wall and the formation of a double layer occurs as depicted in Fig. 1(e). The surface temperature in this case should be large enough for the emitted current to reach the order of the Bohm flux ($0.1-1 n_0 c_s$) and to destabilize the Debye sheath. With the tungsten surface and plasma properties used in the simulations, it corresponds to T_s in the range $2600-2900 \text{ K}$, thanks to Eq. (1). As a result, in the limited regime, ions experience a weaker negative electric field in the sheath region than above the thermal conductivity threshold. Therefore, they impact the wall with a smaller velocity and the sheath size abruptly shrinks to $x/\lambda_d = 1.6$, sheath shrinking which has already been evidenced in Ref. 27.

For $\kappa = 40 \text{ W m}^{-1} \text{ K}^{-1}$, the potential dip built close to the surface due to the double charged layer is large enough to trap ions as seen in the ion phase space [Fig. 4(a)], which induces a reduction of the averaged ion velocity at the wall direct vicinity. In return, their accumulation in this region leads to a small increase in the calculated ion density [see Fig. 1(e)]. This slight ion accumulation has, however, no visible effect on the potential well close to the surface because the large electron density increase due to thermionic emission is disproportionate. It was already mentioned that this trapping phenomenon could occur for instance in the presence of charge-exchange collisions between accelerated ions in the sheath and cold neutrals, or because of increased ionization processes.⁵¹ It could flatten or eventually destroy the potential well, leading to an “inverse sheath,” because of the large ion accumulation possible in this case.^{26,52} This inverse sheath regime due to electron emission has been also investigated in the context of

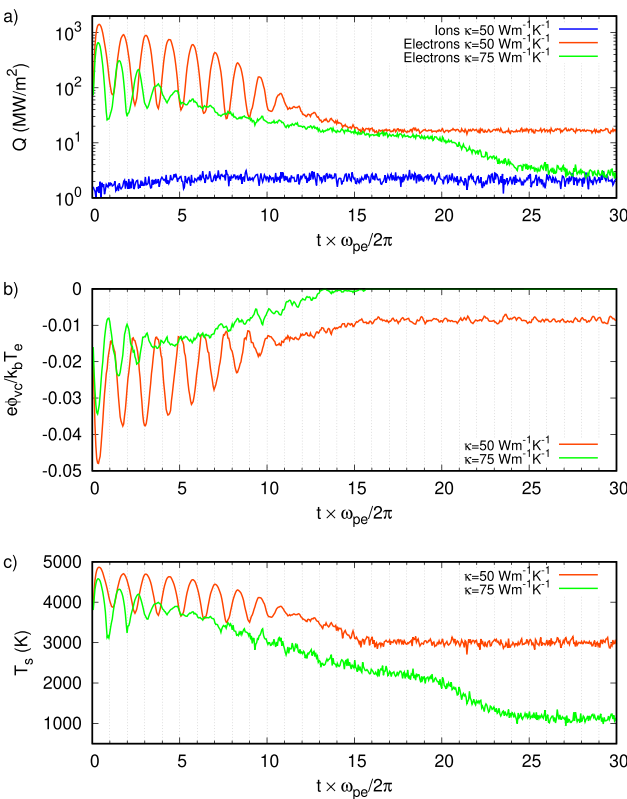


FIG. 2. (a) Time variation of the heat flux from the plasma ion and electron to the wall for different thermal conductivity. (b) Time variation of the virtual cathode potential ϕ_{vc} for $\kappa = 50$ and $75 \text{ W m}^{-1} \text{ K}^{-1}$. (c) Corresponding time variation of the surface temperature.

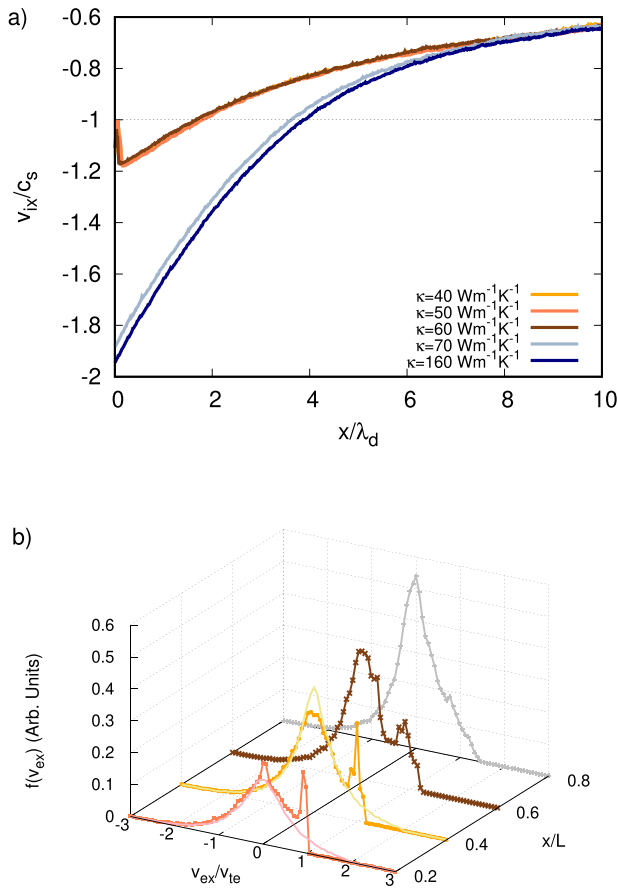


FIG. 3. (a) Spatial variation of the averaged ion velocity v_{ix} . The sheath entrance location is determined at the sonic point $v_{ix} = c_s$. (b) Electron velocity distribution recorded at different plasma locations for $\kappa = 40 \text{ Wm}^{-1} \text{ K}^{-1}$ (line+symbol). At $x/L = 0.2$ and $x/L = 0.4$, the electron velocity distribution is also shown for $\kappa = 160 \text{ Wm}^{-1} \text{ K}^{-1}$ (continuous line).

divertor plasmas⁵³ or radio frequency sheaths.⁴⁹ In our case, there is no collision taken into account, but there is a possibility due to the injection process (ions are deposited everywhere in the plasma according to a uniform distribution in the x direction) that ions with a small velocity compared to c_s appear in the potential dip neighborhood. As this region is quite narrow with respect to the plasma size (0.2 vs 100 λ_d), only a few of them are injected in this area during the simulations. If charge-exchange collisions or realistic ionization procedures taking into account the increased local electron density were used in the PIC simulations, the results may have been different and eventually exhibit an inverse sheath regime as evidenced by other authors.

Concerning the thermionic electrons, they are deposited at the wall with a small velocity with respect to plasma electrons and are eventually accelerated in the sheath, which can be seen in the electron velocity distributions of Fig. 3(b) recorded at different locations in the simulated plasma. For strong thermionic emission, $\kappa = 40 \text{ Wm}^{-1} \text{ K}^{-1}$, a peak clearly visible around $v_{ex}/v_{te} = 0.93$ at $x/L = 0.2$ is due to this electron population. The velocity distribution is also truncated for large positive velocities compared to the one

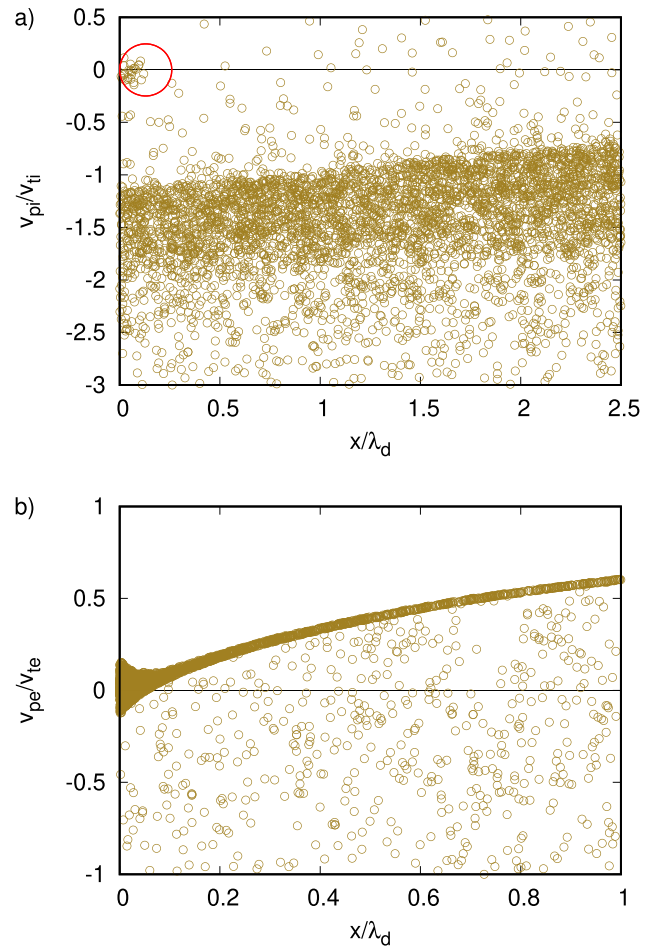


FIG. 4. (a) Ion phase space for a $5 \times 10^{18} \text{ m}^{-3}$ hydrogen plasma with $k_b T_i = k_b T_e = 35 \text{ eV}$ and $\kappa = 40 \text{ Wm}^{-1} \text{ K}^{-1}$. The particles circled in red are those trapped in the potential well evidenced in Fig. 1(b). (b) Electron phase space for the same plasma conditions as in (a).

recorded for $\kappa = 160 \text{ Wm}^{-1} \text{ K}^{-1}$, where the thermionic emission is negligible, and which is shown in the same figure for $x/L = 0.2$ and $x/L = 0.4$ (continuous lines). This missing part of the distribution in the strong emission regime is ascribed to the reduction of the potential drop between the plasma center and the wall exhibited in Fig. 1(a) by almost a factor 5 compared to the non-emitting regime. More plasma electrons with smaller velocity can indeed reach the cathode in this case and disappear from the measured velocity distribution as they are absorbed by the surface. Finally, the effect of the potential well in the surface vicinity is also seen in the electron phase space, Fig. 4(b): a significant part of the emitted electrons goes back to the cathode, while another one corresponding to the space charge limited current is accelerated through the sheath.

B. Heat flux and surface temperature

This increase in the plasma electron flux due to the reduction of the potential drop in the sheath comes along with an augmentation of

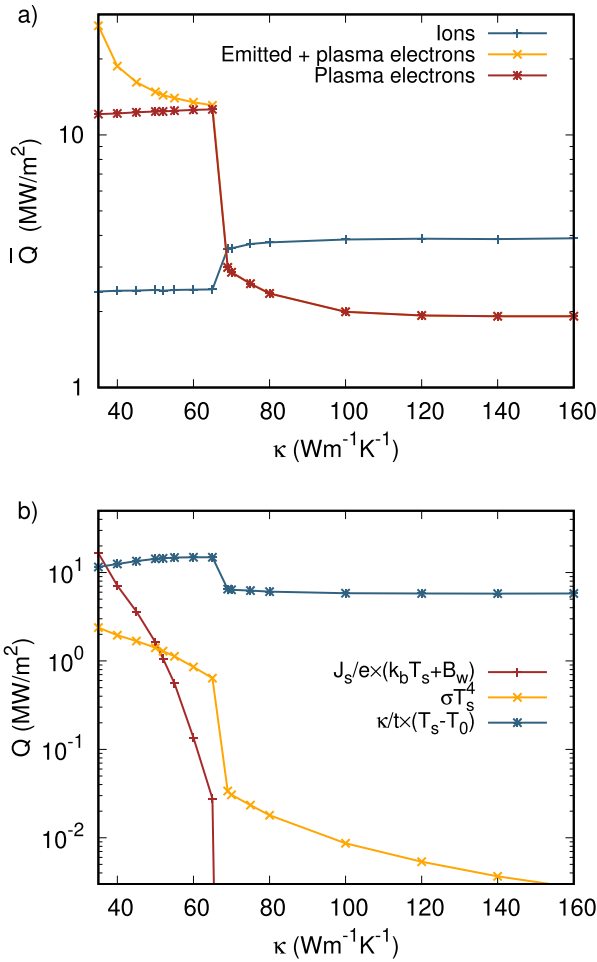


FIG. 5. (a) Average heat flux to the surface due to ions, plasma electrons, and emitted + plasma electrons in the case of a virtual cathode. (b) Heat flux conducted away from the surface due to electrons emission, radiation, and conduction.

their heat flux to the surface, Fig. 5(a), when κ goes down from 160 to 65 $\text{Wm}^{-1}\text{K}^{-1}$. For smaller thermal conductivity, i.e., $\kappa \leq 65 \text{ Wm}^{-1}\text{K}^{-1}$, the system being in the space-charge limited regime, the sheath potential ϕ_s does not vary anymore and neither does the heat flux carried by plasma electrons at the cathode. However, as the surface temperature is expected to keep increasing for smaller κ below this threshold, the number of electrons emitted by the cathode according to the Richardson law J_s is also expected to increase. As the surplus of electrons above the space-charge limited current goes back to the surface, i.e., $J_s - J_s^*$, the total electron (plasma + emitted) heat flux continues increasing as depicted in the figure. The reduction of ϕ_s with κ also implies that the energy gained in the field by ions in the sheath region decreases as well as their heat flux to the wall, Fig. 5(a). In this limited regime also, a large thermionic current J_s^* penetrates the plasma until the right boundary is reached. These emitted electrons are cold with respect to the plasma temperature in our simulations because they are injected at the surface one (less than 1 eV, whereas the plasma is at tens of eV). If these electrons remained

in the system, the overall temperature would decrease. However, thanks to the reflection procedure at the right boundary explained before and the fact their velocity components are reset in the initial Maxwell's distribution, the system can be refurnished in energy and the plasma temperature kept constant for all the set of simulations that we have run.

As explained in Sec. II B, the determination of the surface temperature T_s is achieved by assuming that \bar{Q}_p (the average electron and ion total heat flux to the surface) balances the heat flux conducted away from the surface, given by Eq. (4). The different terms of Eq. (4), i.e., emission of electrons, surface radiation, and heat conduction, are shown in Fig. 5(b) for the same plasma parameters and thermal conductivity than in Fig. 5(a). Most of the heat is evacuated through the wall thickness by conduction. In the space-charge limited regime ($\kappa \leq 65 \text{ Wm}^{-1}\text{K}^{-1}$), a large part of emitted electrons return back to the cathode, which accentuates the heat flux from the plasma to the surface (as stated above) as well as the heat conducted away from it. In fact, each emitted electron carries an energy $k_b T_s$, which will be redeposited entirely onto the surface owing to the virtual cathode (if reflected) balancing both its heat fluxes to and from the cathode. Therefore, in the space charge limited regime, the total heat flux conducted away from the surface due to thermionic emission actually keeps an almost constant value $\equiv \frac{J_s}{e} (k_b T_s + B_w)$ [see Eq. (4)].

The variation of the sheath potential ϕ_s , the surface temperature T_s , and the thermionic current at the surface J_s with respect to κ is depicted in Fig. 6 for the same plasma parameters than previously (a $5 \times 10^{18} \text{ m}^{-3}$ hydrogen plasma with $k_b T_i = k_b T_e = 35 \text{ eV}$) as well as for a hotter one with the same density and $k_b T_i = k_b T_e = 50 \text{ eV}$. A similar trend is observed for both plasma: the sheath potential slowly decreases with κ and then abruptly drops down to its minimal value $\simeq 0.4e\phi_s/T_e$, corresponding to the space charge limited regime where the thermionic current saturates around $3en_0c_s$. The larger the plasma temperature, the larger is the thermal conductivity for which this saturation regime occurs. The surface temperature continuously increases when the thermal conductivity decreases and can reach 3500–3600 K for the lowest κ considered, i.e., 35 and 60 $\text{W m}^{-1}\text{K}^{-1}$ for the 35 and 50 eV plasma, respectively. We did not investigate regimes of κ where the tungsten surface is expected to mold (around 3700 K).

The same general behavior has been evidenced in other simulations in which the electron plasma temperature was increased for a prescribed κ (15 and 100 $\text{W m}^{-1}\text{K}^{-1}$) and for a plasma density and ion temperature of $n_0 = 5 \times 10^{18} \text{ m}^{-3}$ and $k_b T_i = 5 \text{ eV}$, respectively. The electron temperature T_e at which the abrupt transition from the non-emitting regime to the space charge limited regime occurs increases with thermal conductivity, Fig. 7, with a steep augmentation of the thermionic current at the surface still saturating $\simeq 3\text{--}3.2en_0c_s$.

C. Fluid model, bifurcation, and evidence of hysteresis

In order to calculate the heat flux from the plasma to the wall, one needs the potential drop in the sheath ϕ_s with respect to the thermionic current J_s . We based our analyses on the study by Hobbs and Wesson,⁸ who derived the expression of ϕ_s in the presence of electrons emitted at rest on the surface. The authors showed that, even in the presence of thermionic emission, ions keep entering the sheath at a velocity $v_{ix} = v_s$ close to the acoustic velocity c_s , i.e., the Bohm criterion is still valid.⁵⁰ Assuming floating wall conditions, the total current is zero at the wall, which according to Ref. 8 can be written as

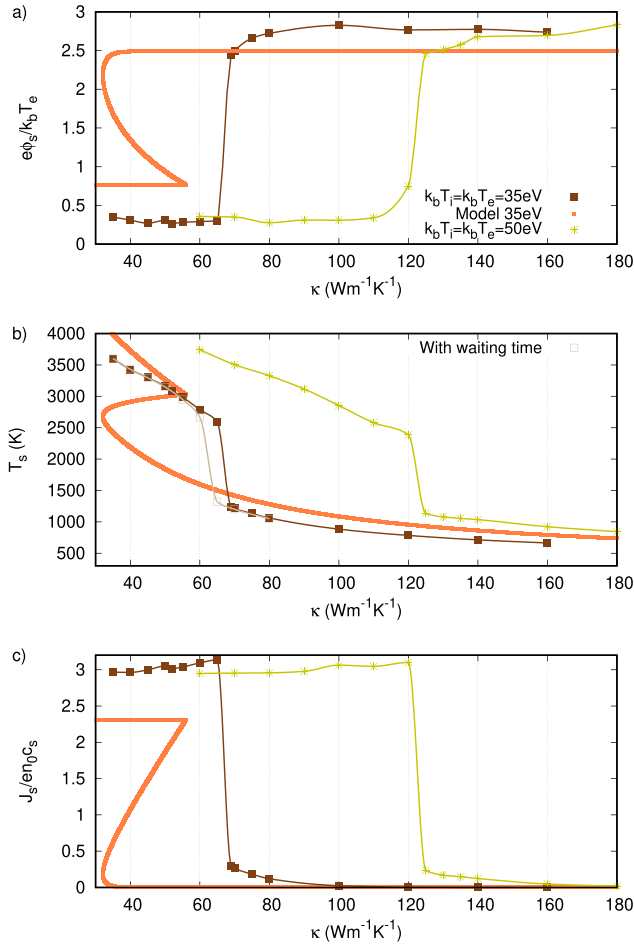


FIG. 6. (a) Variation of the sheath potential ϕ_s , (b) the surface temperature T_s , and (c) the thermionic current at the surface J_s with respect to κ extracted from the PIC simulations and the fluid model of Sec. III C for two plasma conditions. The opened symbols in (b) correspond to the case where a waiting time is used in the beginning of the simulations for $k_b T_i = k_b T_e = 35 \text{ eV}$.

$$n_s v_s + \frac{J_s}{e} = \frac{n_s c_e}{4} \left(1 - \frac{J_s}{e n_s v_{te} \sqrt{\frac{2e\phi_s}{k_b T_e}}} \right) \exp\left(-\frac{e\phi_s}{k_b T_e}\right), \quad (5)$$

with $c_e = \sqrt{\frac{8k_b T_e}{\pi m}}$ and n_s being the plasma density at the sheath entrance.

If the thermionic current is small with respect to $e n_s v_{te}$, substituting $v_s = c_s$ into Eq. (5) leads straightforward to the determination of the sheath potential

$$e\phi_s = e\phi_f - k_b T_e \log\left(1 + \frac{J_s}{e n_s c_s}\right), \quad (6)$$

with ϕ_f being the well-known floating wall potential⁵⁴ given by $-\frac{k_b T_e}{2e} \log(2\pi \frac{m}{M} (1 + \frac{T_i}{T_e}))$. According to Eq. (6), an increase in the thermionic emission leads to a reduction of the sheath potential as

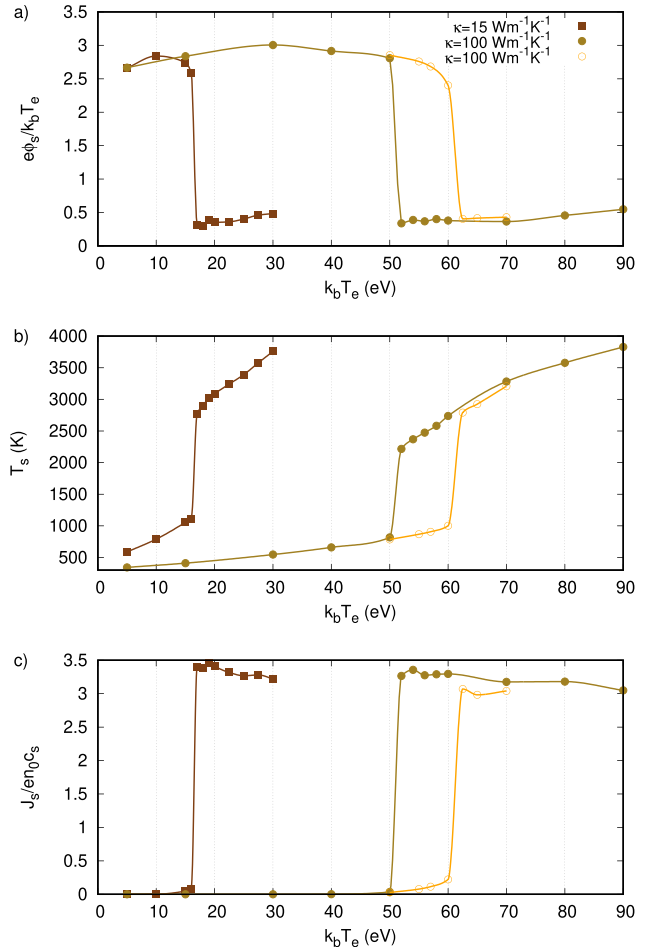


FIG. 7. (a) Variation of the sheath potential ϕ_s , (b) the surface temperature T_s , and (c) the thermionic current at the surface J_s with respect to the electron temperature $k_b T_e$ extracted from the PIC simulations for two values of the thermal conductivity. The hydrogen plasma parameters are $n_0 = 5 \times 10^{18} \text{ m}^{-3}$ and $k_b T_i = 5 \text{ eV}$. The open symbols for the case $\kappa = 100 \text{ Wm}^{-1}\text{K}^{-1}$ correspond to the case where a waiting time is used in the beginning of the simulations.

evidenced in Fig. 6(a) or in Fig. 7(a). However, this reduction cannot go until the disappearance of the sheath, i.e., $\phi_s = 0$, because the electric field at the surface E_s would cancel before for a critical thermionic current J_s^* , marking off the space charge limited regime. As calculated by Hobbs and Wesson, E_s reads

$$\begin{aligned} \frac{\epsilon_0}{2n_0 k_b T_e} E_s^2 = & \frac{M c_s^2}{k_b T_e} \left[\left(1 + \frac{2e\phi_s}{M c_s^2} \right)^{\frac{1}{2}} - 1 \right] \\ & + \left(\exp\left(-\frac{e\phi_s}{k_b T_e}\right) - 1 \right) \left(1 - \frac{J_s}{e n_s v_{te} \sqrt{\frac{2e\phi_s}{k_b T_e}}} \right) \\ & - \frac{J_s}{e n_s v_{te} \sqrt{\frac{2e\phi_s}{k_b T_e}}}. \end{aligned} \quad (7)$$

Thus, for an increasing thermionic current J_s due to an increase in T_s , the potential drop in the sheath ϕ_s can be calculated according to Eq. (6) and then introduced in Eq. (7) until E_s^2 becomes negative and the system enters the space charge limited regime with a minimum ϕ_s^* and a maximum J_s^* .

Once the potential drop in the sheath is known, the heat flux from the plasma to the wall can be calculated as⁵⁵

$$Q_{pf} = \frac{1}{2} n_0 c_s (2k_b T_i + e\phi_s + E_i - B_w) + \frac{n_0 c_e}{8} \exp\left(-\frac{e\phi_s}{k_b T_e}\right) (2k_b T_e + B_w), \quad (8)$$

where we assumed that $n_s = \frac{1}{2} n_0$. In the space charge limited regime, Q_{pf}^* (ϕ_s^*) reaches a maximum, and the heat flux conducted away from the wall, Eq. (4), becomes $Q_c = Q_c(J_s^*)$. In such a regime, the heat flux from the surface due to thermionic emission is maximum, even if T_s increases further, as explained in Sec. III B.

The variation of Q_{pf} with respect to T_s is depicted in Fig. 8(a) for a $n_0 = 5 \times 10^{18} \text{ m}^{-3}$ hydrogen plasma and $k_b T_i = k_b T_e = 35 \text{ eV}$ calculated based on Eqs. (6)–(8). A large increase in Q_{pf} between 2600 and 3000 K occurs and the plasma heat flux to the surface saturates for $T_s > 3000 \text{ K}$ at 17.18 MW m^{-2} . This sudden augmentation of Q_{pf} around 2600 K is ascribed to the decrease in ϕ_s [due to the thermionic current, Eq. (6)], which leads to a large increase in the plasma electron flux reaching the cathode [last term of Eq. (8)].

The determination of the surface temperature is possible by balancing the plasma heat flux to the cathode, Q_{pf} , and conducted away from it, Q_c [Eq. (4)], as shown in Fig. 8(a). It appears that for a large thermal conductivity, $\kappa = 100 \text{ Wm}^{-1} \text{ K}^{-1}$, or a reduced one,

$\kappa = 30 \text{ Wm}^{-1} \text{ K}^{-1}$, the surface reaches a stable low or high temperature. However, there is a range of κ where the equation of $Q_{pf} = Q_c$ does not provide a unique T_s (see $\kappa = 50 \text{ Wm}^{-1} \text{ K}^{-1}$ in the figure). This behavior, already evidenced by other authors,^{15,56,57} leads to a typical S curve of bifurcation where there is a coexistence between a cold and a hot phase of the tungsten surface, associated with the absence or the presence of a strong thermionic emission, respectively, as shown in Fig. 6. The calculated S curves can be seen on the three plotted characteristics, from the sheath potential, the surface temperature to the emitted current crossing the surface, and they are qualitatively in good agreement with the PIC results. It is important to specify that the fluid calculations were carried out with nominal plasma temperatures, which may be different (larger) from the plasma temperatures in the PIC simulations as previously stated. This can explain the differences between the calculated surface temperature and the one from the simulations. Moreover, the transition into the space charge limited regime is calculated in the fluid model from the moment when the electric field on the surface is cancelled, which is not the case in the PIC simulations since a virtual cathode is established in the plasma close to the surface proximity. That is why the calculated ϕ_s^* and J_s^* are larger and smaller, respectively, than the one derived from the PIC simulations. Finally, a similar good agreement is also found between the T_s bifurcation curves calculated for both κ and an increasing electronic plasma temperature T_e , Fig. 8(b), and the PIC results, Fig. 7(b).

In the range of κ (or T_e) where two stable states coexist, it is obvious that the heat flux history matters in determining the final temperature T_s . In order to highlight this effect related to the history and the expected hysteresis associated with it, we have shifted in time the moment when the routine calculating the surface temperature and the number of emitted electrons is called in the code. Until now, this routine was launched at the beginning of the simulations, which led to large electron emission and to the creation of the virtual cathode from the first plasma periods as explained in Sec. III A. Therefore, we introduced in the code a waiting time of $20 \times 2\pi/\omega_{pe}$ before this routine is called—waiting time that is large enough for the sheath to be formed for the working initial condition set—so that the sheath building arises without the effect of thermionic emission. The absence of injected electrons at the wall makes the sheath potential larger and the heat flux due to electrons smaller during the transient state with respect to the case without waiting time, Fig. 9. For a $k_b T_e = 60 \text{ eV}$ plasma ($\kappa = 100 \text{ Wm}^{-1} \text{ K}^{-1}$, $n_0 = 5 \times 10^{18} \text{ m}^{-3}$, and $k_b T_i = 5 \text{ eV}$), the final state of the system clearly depends on its history, i.e., on the temperature reached by the cathode during the transient regime. If the surface experienced transient high heat loads, a virtual cathode is built in its vicinity, and the system remains stuck in this local minimum of the energy until the end of the simulations. If the electron plasma temperature is increased up to $k_b T_e = 70 \text{ eV}$, Fig. 9(b), the waiting time does not change the final state of the system because the heat flux received by the cathode is large enough to make it reach the high temperature regime.

This phenomenon induces a hysteresis on the different characteristics shown in Fig. 7 measured with and without a waiting time: the final T_s depends, for a certain range of T_e , on the history of the cathode, as evidenced by the fluid calculations. Note that the width of the hysteresis is smaller in the PIC simulations than the one expected by the model [compare Fig. 8(b) with Fig. 7(b), for instance]. This can be

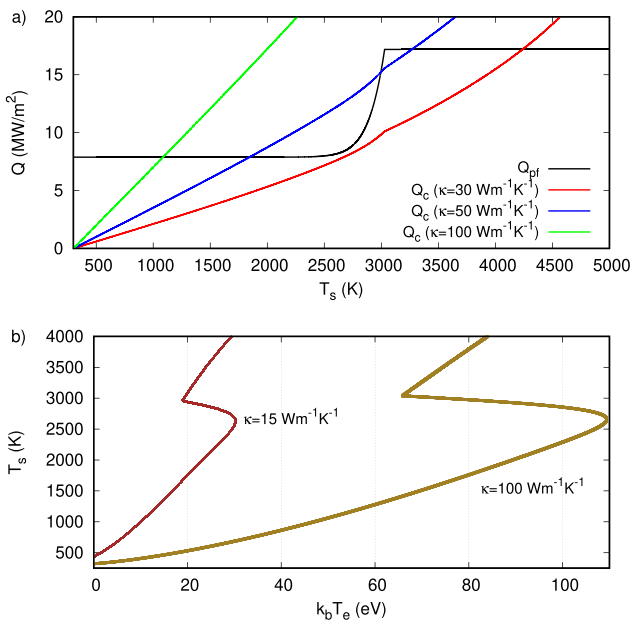


FIG. 8. (a) Calculated heat flux from the plasma to the wall (Q_{pf}) and conducted away from it (Q_c) for three different values of the thermal conductivity. (b) Surface temperature deduced from the fluid model with respect to the plasma electrons' temperature.

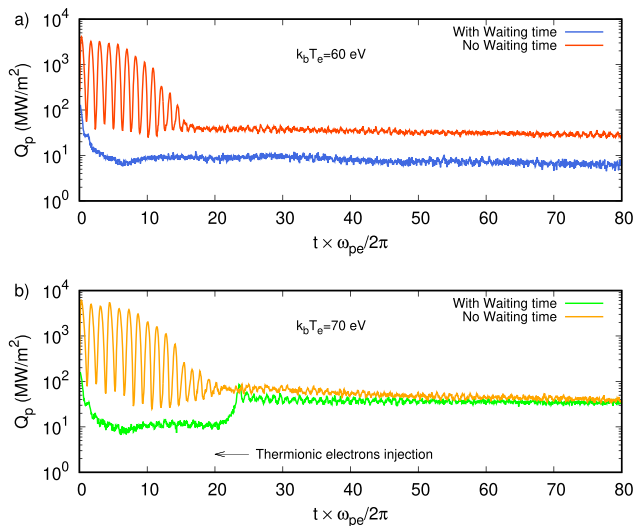


FIG. 9. (a) Time variation of the plasma heat flux to the wall (Q_p) for $k_b T_e = 60$ eV. With the waiting time, the routine calculating the instantaneous surface temperature and the thermionic current to be injected into the plasma at each iteration is run after 20 plasma periods. (b) Same as in (a) for $k_b T_e = 70$ eV.

ascribed to the variation of the heat flux to the surface from one iteration to another. While the fluid calculations are carried out with a constant heat flux to the cathode [Eq. (8)], the kinetic nature of the PIC simulations makes the heat flux vary around an average value. A small deviation of the heat flux associated with the deeply non-linear dependence of the Richardson law on T_s can be enough to change drastically the final situation of the cathode as depicted in Fig. 9(b): in a few iterations, the system transits from a low temperature regime to a space charge limited one. Finally, the same hysteresis phenomenon is present when the simulations are conducted as a function of the thermal conductivity, with and without a waiting time, Fig. 6(b).

IV. CONCLUSION

We have calculated the expected temperature of a tungsten surface T_s facing high heat plasma flux using the PIC simulations. The considered simulated plasma was a dense $5 \times 10^{18} \text{ m}^{-3}$ hydrogen one with various electron and ion temperatures, conditions which can be found in the scrape-off-layer of actual fusion devices.⁵⁸ The heat conducted away from the tungsten surface was due to thermionic emission, surface radiation, and heat conduction through the wall. For each time iteration, the heat flux from the plasma species to the cathode and the one conducted away from it was balanced in order to determine T_s and the number of thermionic electrons to be released in the system. The retained value of T_s was extrapolated at the end of the simulations by considering an average on the heat flux received by the surface. In order to take into account the surface condition, we have varied for each calculation the thermal conductivity, from a value close to a pristine tungsten down to $\kappa = 35 \text{ W m}^{-1} \text{ K}^{-1}$.

When the thermal conductivity κ was decreased, less heat was conducted away through the wall thickness so that the surface temperature was expected to increase. Its rise was at first modest, from a few hundred up to ≈ 1000 K with a negligible thermionic current. However, at a critical κ , whose value depends on plasma conditions (ion and electron

temperature here), the system abruptly transited to a space charge limited regime with a high surface temperature ranging between 2500 and 3000 K. If the thermal conductivity was decreased further, the surface temperature kept increasing, but the plasma sheath potential stayed at a minimum value and the thermionic current penetrating the plasma at a maximum one. It was about three times the Bohm current, which is of the same order of magnitude as the ion current reaching the wall. Other numerical experiments have been carried out for prescribed values of the thermal conductivity (15 and $100 \text{ W m}^{-1} \text{ K}^{-1}$) and an increasing electron plasma temperature, yielding the same conclusions, i.e., a transition from a cold surface temperature to a hot one for which the thermionic current is of the order of magnitude as the Bohm current. For the case of a detached divertor plasma, our simulations showed that, for similar plasma parameters, the space-charge limited regime can be reached only on local defects where the thermal conductivity is quite reduced with respect to the pristine tungsten.

By changing the timing when the routine calculating the surface temperature and the thermionic electron to be injected at the wall at each iteration was launched during the simulations (a waiting time), we have shown that the final state of the system may have changed. With a waiting time, the building of the sheath is achieved without injection of thermo-electrons, and the heat flux to the surface is reduced because the potential drop in the sheath is larger than without a waiting time. The final state of the cathode then depends on its heat flux history, i.e., the temperature it has reached before the steady state is established. We have shown that this hysteresis phenomenon, which has been also evidenced thanks to fluid calculations, arises for a certain range of κ (or T_e). It was very similar to what was already experimentally measured on a tungsten plate⁵⁹ facing a variable and adjustable heat flow of He plasma. It will be interesting to study numerically in the forthcoming future the stability of the sheath subjected to a flux perturbation in order to check whether only one surface temperature solution is stable or both.

Our calculations will be extended soon to the case of magnetized sheaths, where a magnetic field is tilted with respect to the wall, in order to evaluate more precisely the temperature of a divertor surface in the presence of high heat loads^{2,60} although the present calculations can be applied straightforward to misaligned W tiles with a magnetic field perpendicular to the surface, where experiments have already shown that the space-charge limited regime was achievable.⁵

ACKNOWLEDGMENTS

This work was supported by the French National Research Agency (Agence Nationale de la Recherche) under project SHEAR ANR-19-CE30-033-01. It was also carried out within the framework of the French Federation for Magnetic Fusion studies (FR-FCM) and the EUROfusion Consortium, funded by the European Union via the Euratom Research and Training Programme (Grant Agreement No. 101052200 – EUROfusion).

AUTHOR DECLARATIONS

Conflict of Interest

The authors have no conflicts to disclose.

Author Contributions

Jérôme Moritz: Conceptualization (equal); Data curation (equal); Formal analysis (equal); Funding acquisition (equal); Investigation

(equal); Project administration (equal); Software (equal); Writing – original draft (equal). **Stephane Heuraux**: Conceptualization (equal); Investigation (equal); Writing – review & editing (equal). **Nicolas Lemoine**: Conceptualization (equal); Investigation (equal); Validation (equal); Visualization (equal). **Maxime Lesur**: Investigation (equal); Methodology (equal); Software (equal); Validation (equal); Writing – review & editing (equal). **Etienne Gravier**: Formal analysis (equal); Investigation (equal); Writing – review & editing (equal). **Frederic Brochard**: Funding acquisition (equal); Project administration (equal); Writing – review & editing (equal). **Laurent Marot**: Funding acquisition (equal); Project administration (equal); Writing – review & editing (equal). **Paul Huret**: Writing – review & editing (equal).

DATA AVAILABILITY

The data that support the findings of this study are available from the corresponding author upon reasonable request.

REFERENCES

- ¹A. Nedospasov and I. V. Bezyudny, *Contrib. Plasma Phys.* **38**, 337 (1998).
- ²J. Gunn, S. Carpentier-Chouchana, F. Escourbiac, T. Hirai, S. Panayotis, R. Pitts, Y. Corre, R. Dejarnac, M. Firdaouss, M. Kočan, M. Komm, A. Kukushkin, P. Languille, M. Missirlian, W. Zhao, and G. Zhong, *Nucl. Fusion* **57**, 046025 (2017).
- ³R. Pitts, S. Bardin, B. Bazylev, M. van den Berg, P. Bunting, S. Carpentier-Chouchana, J. Coenen, Y. Corre, R. Dejarnac, F. Escourbiac, J. Gaspar, J. Gunn, T. Hirai, S.-H. Hong, J. Horacek, D. Iglesias, M. Komm, K. Krieger, C. Lasnier, G. Matthews, T. Morgan, S. Panayotis, S. Pestchanyi, A. Podolnik, R. Nygren, D. Rudakov, G. De Temmerman, P. Vondracek, and J. Watkins, *Nucl. Mater. Energy* **12**, 60 (2017).
- ⁴J. Coenen, G. Arnoux, B. Bazylev, G. Matthews, A. Autricque, I. Balboa, M. Clever, R. Dejarnac, I. Coffey, Y. Corre, S. Devaux, L. Frassinetti, E. Gauthier, J. Horacek, S. Jachmich, M. Komm, M. Knaup, K. Krieger, S. Marsen, A. Meigs, P. Mertens, R. Pitts, T. Puetterich, M. Rack, M. Stamp, G. Sergienko, P. Tamaïn, V. Thompson, and JET-EFDA Contributors, *Nucl. Fusion* **55**, 023010 (2015).
- ⁵Y. Corre, A. Grosjean, J. P. Gunn, K. Krieger, S. Ratynskaia, O. Skalli-Fettachi, C. Bourdelle, S. Brezinsek, V. Bruno, N. Chanet, J. Coenen, X. Courtois, R. Dejarnac, E. Delmas, L. Delpéch, C. Desgranges, M. Diez, L. Dubus, A. Durif, A. Ekedahl, N. Fedorczak, M. Firdaouss, J.-L. Gardarein, J. Gaspar, J. Gerardin, C. Guillemaut, M. Houry, T. Loarer, P. Maget, P. Mandelbaum, R. Mitteau, M. Missirlian, P. Moreau, R. Nouailletas, E. Nardon, C. Pocheau, A. Podolnik, P. Reilhac, X. Regal-Mezin, C. Reux, M. Richou, F. Rigollet, J.-L. Schwob, E. Thorén, and P. Talias, *E. Tsitrone, and WEST Team, Phys. Scr.* **96**, 124057 (2021).
- ⁶K. Krieger, M. Balden, J. Coenen, F. Laggner, G. Matthews, D. Nille, V. Rohde, B. Sieglin, L. Giannone, B. Göths, A. Herrmann, P. de Marne, R. Pitts, S. Potzel, P. Vondracek, ASDEX-Upgrade Team, and EUROfusion MST1 Team, *Nucl. Fusion* **58**, 026024 (2018).
- ⁷P. Talias, M. Komm, S. Ratynskaia, and A. Podolnik, *Nucl. Fusion* **63**, 026007 (2023).
- ⁸G. D. Hobbs and J. A. Wesson, *Plasma Phys.* **9**, 85 (1967).
- ⁹J. Ou and X. Zhao, *Contrib. Plasma Phys.* **57**, 50 (2017).
- ¹⁰L. A. Schwager, W. L. Hsu, and D. M. Tung, *Phys. Fluid B* **5**, 621 (1993).
- ¹¹C. Herring and M. H. Nichols, *Rev. Mod. Phys.* **21**, 185 (1949).
- ¹²M. Y. Ye, S. Masuzaki, K. Shiraiishi, S. Takamura, and N. Ohno, *Phys. Plasmas* **3**, 281 (1996).
- ¹³D. F. Johnson and E. A. Carter, *J. Mater. Res.* **25**, 315 (2010).
- ¹⁴V. Philipps, U. Samm, M. Z. Tokar, B. Unterberg, A. Pospieszczyk, and B. Schweer, *Nucl. Fusion* **33**, 953 (1993).
- ¹⁵R. D. Smirnov, S. I. Krasheninnikov, and A. Y. Pigarov, *Phys. Plasmas* **16**, 122501 (2009).
- ¹⁶F. R. Schwirzke, *IEEE Trans. Plasma Sci.* **19**, 690 (1991).
- ¹⁷S. A. Barengolts, G. A. Mesyats, and M. M. Tsventoukh, *Nucl. Fusion* **50**, 125004 (2010).
- ¹⁸C. D. Child, *Phys. Rev. (Series I)* **32**, 492 (1911).
- ¹⁹I. Langmuir, *Phys. Rev.* **2**, 450 (1913).
- ²⁰M. S. Benilov, *Plasma Sources Sci. Technol.* **18**, 014005 (2009).
- ²¹J. Moritz, S. Heuraux, E. Gravier, M. Lesur, F. Brochard, L. D. Poucques, E. Faudot, and N. Lemoine, *Phys. Plasmas* **28**, 083501 (2021).
- ²²G. Porter, *Nucl. Fusion* **22**, 1279 (1982).
- ²³L. A. Schwager, *Phys. Fluid B* **5**, 631 (1993).
- ²⁴S. Takamura, N. Ohno, and M. Y. T. Kuwabara, *Contrib. Plasma Phys.* **44**, 126 (2004).
- ²⁵J. Cavalier, N. Lemoine, G. Bousselin, N. Plihon, and J. Ledig, *Phys. Plasmas* **24**, 013506 (2017).
- ²⁶M. Campanell, *Phys. Rev. E* **97**, 043207 (2018).
- ²⁷N. Ohno, E. Shimizu, and S. Takamura, *Contrib. Plasma Phys.* **36**, 386 (1996).
- ²⁸T. Gyergyek and J. Kovačič, *Contrib. Plasma Phys.* **53**, 189 (2013).
- ²⁹M. Komm, S. Ratynskaia, P. Talias, J. Cavalier, R. Dejarnac, J. P. Gunn, and A. Podolnik, *Plasma Phys. Controlled Fusion* **59**, 094002 (2017).
- ³⁰T. Hirai, S. Panayotis, V. Barabash, C. Amzallag, F. Escourbiac, A. Durocher, M. Merola, J. Linke, T. Loewenhoff, G. Pintsuk, M. Wirtz, and I. Uytendhouwen, *Nucl. Mater. Energy* **9**, 616 (2016).
- ³¹E. L. Murphy and R. H. Good, Jr., *Phys. Rev.* **102**, 1464 (1956).
- ³²T. Rognlien, A. McLean, M. Fenstermacher, M. Groth, A. Jaervinen, I. Joseph, C. Lasnier, W. Meyer, A. Moser, G. Porter, and M. Umansky, *Nucl. Mater. Energy* **12**, 44 (2017).
- ³³T. Takizuka, M. Hosokawa, and K. Shimizu, *J. Nucl. Mater.* **290**, 753 (2001).
- ³⁴V. P. Gopinath, J. P. Verboncoeur, and C. K. Birdsall, *Phys. Plasmas* **5**, 1535 (1998).
- ³⁵J. Moritz, M. Lesur, E. Faudot, S. Devaux, S. Heuraux, and J. Ledig, *Phys. Plasmas* **26**, 013507 (2019).
- ³⁶R. Bisswell, P. Johnson, and P. Stangeby, *Phys. Fluid B* **1**, 1133 (1989).
- ³⁷P. C. Stangeby, *The Plasma Boundary of Magnetic Fusion Devices* (Institute of Physics Publishing, London, 2000), p. 73.
- ³⁸D. Tskhakaya and S. Kuhn, *J. Nucl. Mater.* **313**, 1119 (2003).
- ³⁹A. Gallo, A. Sepety, J. Romazanov, Y. Marandet, S. Brezinsek, H. Bufferand, G. Ciraolo, Y. Corre, S. Ertmer, N. Fedorczak, J. Gunn, A. Kirschner, C. Martin, O. Meyer, G. J. van Rooij, P. Roubin, and E. Tsitrone, EUROfusion PFC Team, and WEST Team, *Phys. Scr.* **2020**, 014013.
- ⁴⁰D. Tskhakaya, S. Jachmich, T. Eich, and W. Fundamenski, *J. Nucl. Mater.* **415**, S860 (2011).
- ⁴¹J. Gaspar, C. Pocheau, Y. Corre, N. Ehret, D. Guilhem, M. Houry, T. Loarer, T. Loewenhoff, C. Martin, C. Pardanaud, G. Pintsuk, M. Richou, F. Rigollet, H. Roche, G. Sepulcre, and M. Wirtz, *Fusion Eng. Des.* **149**, 111328 (2019).
- ⁴²P. Talias, *Nucl. Mater. Energy* **13**, 42 (2017).
- ⁴³S. Cui, M. Simmonds, W. Qin, F. Ren, G. R. Tynan, R. P. Doerner, and R. Chen, *J. Nucl. Mater.* **486**, 267 (2017).
- ⁴⁴H. Zhang, J. Sun, Y. Wang, T. Stirner, A. Y. Hamid, and C. Sang, *Fusion Eng. Des.* **161**, 112004 (2020).
- ⁴⁵D. Hasselman, *J. Compos. Mater.* **12**, 403 (1978).
- ⁴⁶I. Langmuir, *Phys. Rev.* **2**, 329 (1913).
- ⁴⁷H. A. Jones, I. Langmuir, and G. M. J. Mackay, *Phys. Rev.* **30**, 201 (1927).
- ⁴⁸M. D. Campanell and M. V. Umansky, *Phys. Rev. Lett.* **116**, 085003 (2016).
- ⁴⁹G.-Y. Sun, A.-B. Sun, and G.-J. Zhang, *Phys. Rev. E* **101**, 033203 (2020).
- ⁵⁰D. Bohm, *The Characteristics of Electrical Discharges in Magnetic Fields*, edited by A. Guthrie and R. K. Wakerling (McGraw-Hill, New York, 1949), p. 77.
- ⁵¹T. Intrator, M. H. Gilo, E. Y. Wang, N. Hershkovitz, D. Diebold, and J. DeKock, *J. Appl. Phys.* **64**, 2927 (1988).
- ⁵²M. Campanell, *Phys. Rev. E* **88**, 033103 (2013).
- ⁵³R. Masline, R. Smirnov, and S. Krasheninnikov, *Phys. Plasmas* **27**, 092505 (2020).
- ⁵⁴P. Stangeby, *Nucl. Fusion* **52**, 083012 (2012).

- ⁵⁵E. Hantzsche, in *Handbook of Vacuum Arc Science and Technology*, edited by R. L. Boxman, D. M. Sanders, and P. J. Martin (William Andrew Publishing, Park Ridge, NJ, 1996), pp. 151–208.
- ⁵⁶S. Takamura, N. Ohno, K. Shiraishi, and S. Masuzaki, *J. Nucl. Mater.* **196**, 448 (1992).
- ⁵⁷M. Tokar, A. Nedospasov, and A. Yarochkin, *Nucl. Fusion* **32**, 15 (1992).
- ⁵⁸X. Zhang, F. Poli, E. Emdee, and M. Podest, *Nucl. Mater. Energy* **34**, 101354 (2023).
- ⁵⁹M. Y. Ye, S. Takamura, and N. Ohno, *J. Nucl. Mater.* **241**, 1243 (1997).
- ⁶⁰R. Delaporte-Mathurin, H. Yang, J. Denis, J. Dark, E. A. Hodille, G. D. Temmerman, X. Bonnin, J. Mougenot, Y. Charles, H. Bufferand, G. Ciraolo, and C. Grisolia, *Nucl. Fusion* **61**, 126001 (2021).